Petroleum Science 21 (2024) 182–194

Contents lists available at ScienceDirect

Petroleum Science

journal homepage: www.keaipublishing.com/en/journals/petroleum-science

Original Paper

A stable staggered-grid finite-difference scheme for acoustic modeling beyond conventional stability limit

Jing-Yi Xu [a], Yang Liu [a, b, *]

[a] National Key Laboratory of Petroleum Resources and Engineering, China University of Petroleum (Beijing), Beijing 102249, China
[b] China University of Petroleum (Beijing), Karamay Campus, Karamay 834000, Xinjiang, China

ARTICLE INFO

Article history:
Received 5 February 2023
Received in revised form
11 July 2023
Accepted 11 September 2023
Available online 18 September 2023

Edited by Jie Hao and Meng-Jiao Zhou

Keywords:
Acoustic wave
Staggered-grid finite-difference (SGFD) modeling
Courant-friedrichs-lewy (CFL) number
Stability

ABSTRACT

Staggered-grid finite-difference (SGFD) schemes have been widely used in acoustic wave modeling for geophysical problems. Many improved methods are proposed to enhance the accuracy of numerical modeling. However, these methods are inevitably limited by the maximum Courant-Friedrichs-Lewy (CFL) numbers, making them unstable when modeling with large time sampling intervals or small grid spacings. To solve this problem, we extend a stable SGFD scheme by controlling SGFD dispersion relations and maximizing the maximum CFL numbers. First, to improve modeling stability, we minimize the error between the FD dispersion relation and the exact relation in the given wave-number region, and make the FD dispersion approach a given function outside the given wave-number area, thus breaking the conventional limits of the maximum CFL number. Second, to obtain high modeling accuracy, we use the SGFD scheme based on the Remez algorithm to compute the FD coefficients. In addition, the hybrid absorbing boundary condition is adopted to suppress boundary reflections and we find a suitable weighting coefficient for the proposed scheme. Theoretical derivation and numerical modeling demonstrate that the proposed scheme can maintain high accuracy in the modeling process and the value of the maximum CFL number of the proposed scheme can exceed that of the conventional SGFD scheme when adopting a small maximum effective wavenumber, indicating that the proposed scheme improves stability during the modeling.

1. Introduction

Numerical simulation of the seismic wave equation is of great significance in seismic exploration. The accuracy and efficiency of imaging (Etgen et al., 2009; Baysal et al., 1983; McMechan, 1983; Yan and Sava, 2008; Feng and Schuster, 2017) and inversion (Virieux and Operto, 2009; Tarantola, 1984; Vigh et al., 2014) are largely determined by the forward numerical modeling algorithms. Among various numerical algorithms, the finite-difference (FD) method has gained popularity due to its simplicity and low computational cost (Alford et al., 1974; Kelly et al., 1976; Virieux, 1984, 1986; Dablain, 1986; Levander, 1988; Liu and Sen, 2011; Yang et al., 2014; Bansal and Sen, 2008). When applying the FD method to solve wave equations, it is essential to discretize spatial and temporal derivatives, leading to temporal and spatial dispersion as well as phase velocity errors (Dablain, 1986; Holberg, 1987; Fornberg, 1988; Tam and Webb, 1993; Liu and Sen, 2009). Consequently, some false appearances may occur in the profile, such as out-of-phase axis focus, reduction in resolution, and deviation of the reflection interface from its actual position (Ren et al., 2021). In addition to the issues mentioned above, the FD method may suffer from instability during modeling due to the maximum Courant-Friedrichs-Lewy (CFL) number limit (Robertsson et al., 1994; Gaffar and Jiao, 2014; Amundsen and Pedersen, 2017). Specifically, when velocity model and grid spacing are given, the wavefield cannot be modeled with a large time sampling interval for a long propagation time. It is feasible to increase grid spacing or reduce time sampling interval, whereas causes increased numerical dispersion and computational cost. In summary, it is necessary to reduce dispersion errors and improve stability when using the FD method for seismic modeling.

A common method for conveniently and effectively reducing spatial dispersion is to adjust the spatial FD coefficients. Among all approaches for computing these coefficients, the Taylor-series expansion (TE) method (Liu and Sen, 2009, 2013; Liu et al., 2014)

* Corresponding author. National Key Laboratory of Petroleum Resources and Engineering, China University of Petroleum (Beijing), Beijing 102249, China.
E-mail address: wliuyang@vip.sina.com (Y. Liu).

https://doi.org/10.1016/j.petsci.2023.09.009

is widely implemented with high computational efficiency, small memory footprints and high accuracy. However, the TE method produces large FD dispersion errors in large wavenumber areas and requires a longer operator to meet accuracy requirements, leading to substantial computational cost. Furthermore, as the operator becomes longer, the accuracy might be limited by the "saturation effect" (Kosloff et al., 2010). An effective way to handle this problem is to adopt optimization methods to calculate the FD coefficients. These optimization methods establish an objective function by adopting either the two-norm (Zhou and Zhang, 2011; Wang et al., 2016; Liu, 2013) or the maximum norm (Holberg, 1987; Kindelan et al., 1990; Zhang and Yao, 2013a, 2013b) and minimize the errors of phase (Jing et al., 2017) or group (Holberg, 1987) velocities or dispersion relations within the designated bandwidth and operator length. When utilizing the two-norm to establish an objective function, the least-squares (LS) approximation can be used to solve for the optimal FD coefficients in both the spatial and temporal domains by minimizing the relative error within a given range of wavenumbers (Liu, 2013, 2014; Wang et al., 2016). Compared with the TE method, the LS method broadens the effective wavenumber range and improves FD accuracy with moderate computational costs. Additionally, Jing et al. (2017) adopt the LS method in the wavenumber domain based on stereo-modeling (SMD) operators to obtain optimal constant coefficients that approximate high-order spatial partial derivatives. This method can effectively suppress numerical dispersion even on extremely coarse grids, and can even surpass the Nyquist sampling rate limit with small computational errors. Ma and Yang (2017) employ the SMD operator for spatial discretization and optimized the coefficients of symplectic partitioned Runge-Kutta methods by minimizing phase errors. This approach avoids phase drifts after long-term iterations and ensures modeling stability. However, because of the limitation of the objective function form and situations where optimal solutions are not available, the LS method may sometimes be inflexible and unsuitable (Chen et al., 2016b; Zhang and Yao, 2013a). In contrast, using the maximum norm to establish an objective function leads to tighter error limitations and greater flexibility (Zhang and Yao, 2013a; Holberg, 1987). Yang et al. (2017) optimizes spatial staggered-grid finite difference (SGFD) coefficients through the Remez exchange algorithm (REA) and achieves high numerical accuracy over a wide bandwidth range. After two or three iterations, the spatial SGFD coefficients converge to equal-ripple solutions, resulting in the widest bandwidth coverage among the methods mentioned above with high numerical precision (He et al., 2019). Liu (2020a) and Wang et al. (2021) develop the REA on variable-length explicit and implicit FD schemes, respectively. They adopt shorter operators than conventional methods, resulting in further decreased computational time. Therefore, the REA is an effective way to obtain a wider wavenumber area and higher accuracy.

Among all kinds of methods to improve stability of the FD method, a straightforward approach is to enhance temporal accuracy. There are mainly two kinds of methods to increase temporal accuracy and thus improve stability. The first kind is the Lax-Wendroff (LW) method (Dablain, 1986; Chen, 2007; Long et al., 2013). The LW method improves stability and accuracy of modeling by replacing the high-order terms of temporal derivatives with spatial derivatives (Long et al., 2013), whereas causing a huge computational cost. The second kind is the time-space domain FD scheme. Liu and Sen (2009) propose an FD scheme that approximates both spatial and temporal derivatives simultaneously, achieving up to (2 M)th-order accuracy along eight specific propagation directions in the 2D case. To further improve temporal FD accuracy and modeling stability, Liu and Sen (2013) develop a rhombus scheme, which reaches (2 M)th-order arbitrary even-order accuracy along all directions. Though the rhombus scheme provides significantly high accuracy, its computational cost increases significantly with longer operators. Wang et al. (2016) combine the cross scheme and the rhombus scheme to balance accuracy and efficiency. Later, Liu (2020a) extends this combination scheme to the SGFD method. Meanwhile, inspired by the rhombus scheme (Tan and Huang, 2014; Liu and Sen, 2013), Ren and Li (2017) and Chen et al. (2016a) propose an off-axial rhombus SGFD scheme modeling elastic wavefield, which obtains high-order temporal and spatial accuracies, whereas costs expensively owing to adding many extra off-axial points. To tackle the issue, an effective temporal and spatial high-accuracy elastic SGFD scheme is proposed and distinguishes itself for its high accuracy and low computational consumption, which selectively adds off-axial rhombus points to the original SGFD scheme (Zhou et al., 2021b). To simulate wave propagation more stably, Zhou et al. (2021a) recombine the temporal and the spatial operators by setting the length of the rhombus operators to exceed the length of the cross operators, which breaks the conventional stability limit. Time–space domain methods can effectively reduce temporal dispersion and improve simulation stability. However, during simulations, different FD coefficients need to be calculated for different CFL numbers, which greatly increases computation time. To address this issue, Chen et al. (2016c) develop a 3D time–space domain stereo finite difference method for wave equation forward modeling. This method propagates both displacement and displacement gradient simultaneously that preserving more wavefield information, and uses constant FD coefficients to adapt to changes in CFL number. Consequently, it suppresses numerical dispersion effectively and reduces computation time significantly. Essentially, it is also significantly feasible and effective to adopt perturbation methods to adjust eigenvalues and make the modeling stable (Gaffar and Jiao, 2014, 2015; Gao et al., 2018, 2019). However, this kind of method has difficulty in processing extremely large 2D models and moderate 3D models, making it unrealistic to be applied in real data.

Besides the aforementioned methods to improve stability, Liu (2020b, 2022) exploits a new method that controls dispersion relations and maximizes the CFL number to obtain regular-grid FD coefficients of the second-order acoustic wave equation. This method maintains modeling accuracy and breaks up conventional stability limit. Motivated by this idea, we develop a new SGFD method to solve the first-order acoustic wave equation. This new method approximates dispersion relations to the exact relations inside the given wavenumber area and approaches a given function outside the given area, respectively. Compared with the conventional SGFD method, the new method has better stability, especially in the situation of adopting a small maximum effective wavenumber. In addition, we use the REA and the time-dispersion correction strategy (Koene et al., 2018; Liu, 2020a; Finkelstein and Kastner, 2008) to reduce spatial and temporal dispersions respectively. The hybrid absorbing boundary condition (HABC) (Liu and Sen, 2010, 2018; Zhao et al., 2019) is adopted to reduce artificially reflected waves generated from the model boundary. After testing, we obtain an optimal weighting coefficient for HABC in the new method. The effectiveness of the new method can be demonstrated by dispersion analysis, stability analysis, and numerical examples.

2. Methodology

In this section, we first introduce how to obtain FD coefficients through the REA and deduce the stability requirements for the conventional SGFD scheme. Then we elaborate in detail on the new method.

2.1. Conventional SGFD scheme for 2D acoustic wave equation

We express the 2D acoustic wave equation with first-order spatial derivatives with variable density in homogeneous media as follows (Liu and Sen, 2011):

$$\frac{\partial}{\partial x}\left(\frac{1}{\rho}\frac{\partial p}{\partial x}\right)+\frac{\partial}{\partial z}\left(\frac{1}{\rho}\frac{\partial p}{\partial z}\right)=\frac{1}{K}\frac{\partial^2 p}{\partial t^2} \tag{1}$$

where $p=p(x,z,t)$ is the acoustic wavefield, $K=\rho v^2$ is the bulk modulus, ρ and v represent the density and the velocity of the modeling model, respectively.

The (2M)th-order SGFD scheme and a second-order formula are applied to solve the first-order spatial derivative and the second-order temporal derivative, respectively. The derivatives are expressed as (Liu and Sen, 2011; Ren and Liu, 2015):

$$\frac{\partial p}{\partial x}\approx\frac{1}{h}\sum_{m=1}^{M}c_m\left(p^0_{m-1/2,0}-p^0_{-m+1/2,0}\right) \tag{2}$$

$$\frac{\partial p}{\partial z}\approx\frac{1}{h}\sum_{m=1}^{M}c_m\left(p^0_{0,m-1/2}-p^0_{0,-m+1/2}\right) \tag{3}$$

$$\frac{\partial^2 p}{\partial t^2}\approx\frac{p^1_{0,0}+p^{-1}_{0,0}-2p^0_{0,0}}{\tau^2} \tag{4}$$

where τ and h stand for time step and grid size, respectively. M is the operator length of the spatial FD scheme, and c_m represents the spatial FD coefficient. $p^n_{m,j}=p(x+mh,z+jh,t+n\tau)$ is defined as the plane-wave solution (Liu and Sen, 2009), and

$$p^n_{m,j}=e^{\mathrm{i}(k_x(x+mh)+k_z(z+jh)-\omega(t+n\tau))} \tag{5}$$

where, i means the imaginary unit, $k_x=k\cos\theta$ and $k_z=k\sin\theta$ are wavenumbers along x- and z-directions, respectively. k denotes wavenumbers, θ is the angle between the wave propagation direction and the positive direction of the x-direction, and ω stands for the angular frequency.

Substitute Eqs. (2)–(4) into Eq. (1) and derive the following recursive equation (Liu and Sen, 2011; Ren and Liu, 2015):

$$\begin{aligned}p^1_{0,0}=&2p^0_{0,0}-p^{-1}_{0,0}+r^2\sum_{m=1}^{M}\sum_{n=1}^{M}c_mc_n\left(p^0_{m+n-1,0}-p^0_{m-n,0}\right)\\&+r^2\sum_{m=1}^{M}\sum_{n=1}^{M}c_mc_n\left(\left(p^0_{-m+n,0}-p^0_{-m-n+1,0}\right)\right)\\&+r^2\sum_{m=1}^{M}\sum_{n=1}^{M}c_mc_n\left(p^0_{0,m+n-1}-p^0_{0,m-n}\right)\\&+r^2\sum_{m=1}^{M}\sum_{n=1}^{M}c_mc_n\left(\left(p^0_{0,-m+n}-p^0_{0,-m-n+1}\right)\right)\end{aligned} \tag{6}$$

where $r=v\tau/h$ is the CFL number.

By substituting Eq. (5) into Eq. (6) and expanding the trigonometric terms using Taylor series, the conventional TE-based FD coefficients can be obtained (Liu and Sen, 2009, 2011).

To obtain the dispersion relation equation of the SGFD method, we can substitute Eq. (5) into Eq. (2) and Eq. (3), and replace $\beta_x=k_xh$ and $\beta_z=k_zh$ with β, $\beta_x,\beta_z\in[0,\pi]$, then acquire the following equations:

$$\varphi(\beta)\approx\beta \tag{7}$$

and

$$\varphi(\beta)=2\sum_{m=1}^{M}c_m\sin[(m-0.5)\beta] \tag{8}$$

where β ranges from 0 to B, and $B=2\pi f_{\max}h/v$, $f_{\max}$ stands for the maximum effective frequency.

The process of seeking optimal FD coefficients aims to minimize the absolute error $\varepsilon_{\mathrm{abs}}(\beta)$ or relative error $\varepsilon_{\mathrm{rel}}(\beta)$ of the spatial dispersion relation in Eq. (7). These errors can be represented as follows (Liu, 2013, 2014, 2020a):

$$\varepsilon_{\mathrm{abs}}(\beta)=\varphi(\beta)-\beta \tag{9}$$

and

$$\varepsilon_{\mathrm{rel}}(\beta)=\varphi(\beta)/\beta-1 \tag{10}$$

Note that, for acoustic SGFD modeling in the small wavenumber area, minimizing the relative error of the space-domain dispersion relation can obtain better accuracy than calculating the absolute error (Liu, 2013). Therefore, we use the relative error to obtain optimized finite difference coefficients.

By using the idea of REA (Liu, 2020a; Yang et al., 2016; Wang et al., 2021), the objective function is defined by applying the maximum norm. According to Eq. (10), the objective function is supposed as follows:

$$|\varphi(\beta)/\beta-1|\le\eta,\beta\in[0,B] \tag{11}$$

where B is the maximum effective value of β and η stands for a constant that we set to limit the maximum error. This objective function will guarantee the accuracy within the given range $[0,B]$, making sure that the relative error will not exceed the limit of the maximum error η. According to the REA, we define

$$\varepsilon_{\mathrm{rel}}(\beta)=(-1)^iE,\ i=1,\ 2,\ \ldots,\ M+1 \tag{12}$$

where E is a variable constant to represent the equal-ripple error.

Combining Eqs. (8), (10) and (12), we deduce the following linear equations (Liu, 2020a):

$$A[c_1,c_2,\ldots,c_M,E]^{\mathrm{T}}=[d_1,d_2,\ldots,d_M,d_{M+1}] \tag{13}$$

where,

$$A_{i,j}=\begin{cases}2\sin[(j-0.5)\beta_i]/\beta_i, & 1\le j\le M\\(-1)^{i+1}, & j=M+1\end{cases} \tag{14}$$

$$d_i=1,1\le i\le M+1 \tag{15}$$

and β_i is a series of equally spaced points in the first iteration or extreme points in another iteration. We can use the Gaussian elimination method or some other methods to solve this linear Eq. (13). During the iteration, exchange extreme points and recalculate Eq. (13) until the FD coefficients meet the requirement of accuracy. Generally, it will take only two or three iterations to reach the requirement of accuracy in a given wavenumber region.

Fig. 1a displays variations of $\varphi(\beta)$ with β from the TE method and the REA, it can be seen that these two methods provide the same variations, i.e., $\varphi(\beta)$ increases with the increase of β when $0\le\beta\le\pi$. $\varphi(\beta)$ almost equals β in the small wavenumber area and when the value of β is bigger than B, the curve of $\varphi(\beta)$ gradually

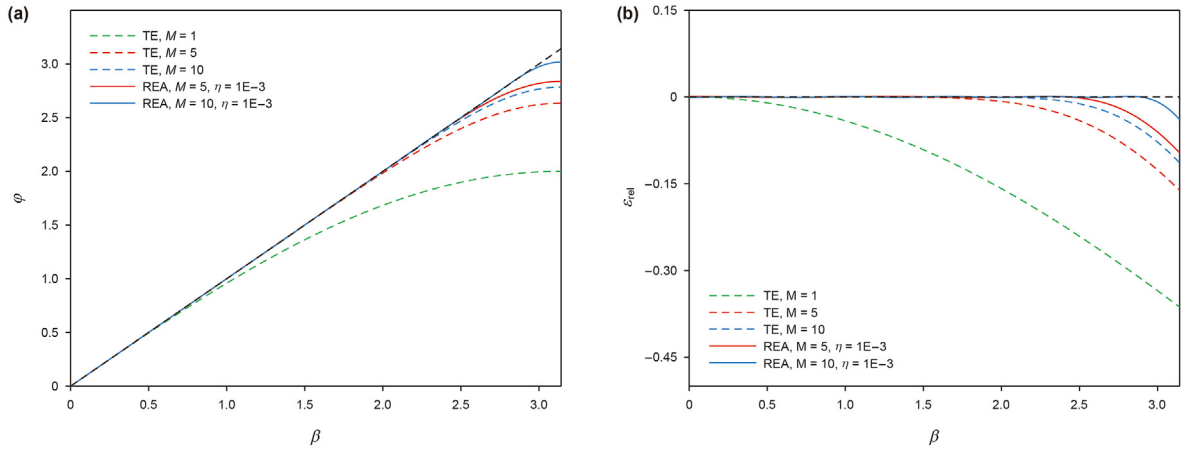

Fig. 1. Variations of (a) φ and (b) ε_{rel} with β for different values of M from the TE and the REA. $\eta = 1\text{E}-3$.

deviates far away from the curve of β as β increases. We can increase the operator length M to increase B. Fig. 1a also displays the influence to $\varphi(\beta)$ for different values of M, i.e., as M increases, B will be closer to π in the large wavenumber area. Fig. 1b illustrates the corresponding variations of the relative error $\varepsilon_{\text{rel}}(\beta)$. It can be observed that as M increases, the relative error will become smaller when $\beta \leq B$, and the REA can acquire higher accuracy results than the TE method when using the same length of the operators. However, as $\beta > B$, the relative error increases dramatically, which demonstrates that the modeling becomes unstable. To compare with the new method, we name the REA as the conventional method.

2.2. Stability analysis for the conventional SGFD schemes

2D stability condition for the conventional SGFD method can be expressed as (Liu and Sen, 2011):

$$r \leq r_{\max} = \left(\sqrt{2} \sum_{m=1}^{M} |c_m| \right)^{-1} \tag{16}$$

which means the modeling will be stable when the CFL number is smaller than the maximum CFL number $r_{\max}$.

When $M = 1$, $c_1 = 1$,

$$r_{\max} = 1 \Big/ \sqrt{2} \approx 0.707 \tag{17}$$

When M approaches infinity and B approaches π,

$$r_{\max} = \sqrt{2} \Big/ \pi \approx 0.450 \tag{18}$$

The variations of $r_{\max}$ with M can also be concluded from Fig. 2. It can be observed that $r_{\max}$ decreases with the increase of M from about 0.707 to 0.450, and the stability of the TE method is better than that of the REA.

2.3. A new method for determining spatial SGFD coefficients by controlling the dispersion relation

According to Eq. (A-9) in Appendix A, it can be concluded that $r_{\max}$ depends on the maximum value of $\varphi(\beta)$. As we know in Fig. 1a, $\varphi(\beta)$ approaches β when $0 \leq \beta \leq B$. Though we can change the method or increase M to increase B, there still exists a situation when β is larger than M, $\varphi(\beta)$ no longer approaches β and the value

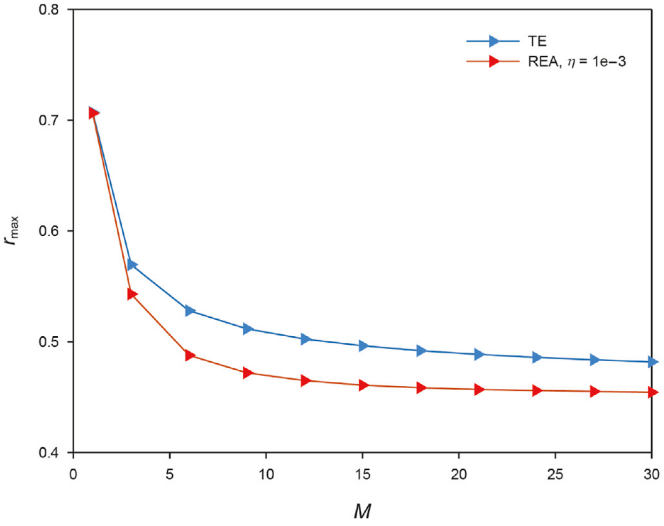

Fig. 2. Variations of $r_{\max}$ with M from the TE method and the REA.

of $\varphi(\beta)$ is not able to be estimated intuitively.

We define a function $f(\beta)$ and let $\varphi(\beta)$ approach the $f(\beta)$ in the interval $[B + \Delta\beta, \pi]$. Corresponding to Eq. (26) in Liu (2020b), the objective function is set as following:

$$|\varphi(\beta) / \beta - f(\beta)| \leq b\eta \tag{19}$$

where, b is a constant, and this given function $f(\beta)$ is expressed as

$$f(\beta) = B/\beta \tag{20}$$

To sum up, we construct a new Eq. (19) and combine it with Eq. (11), then the objective function of the new method can be written as:

$$\begin{cases} |\varphi(\beta)/\beta - 1| \leq \eta, \ 0 \leq \beta \leq B \\ |\varphi(\beta)/\beta - f(\beta)| \leq b\eta, \ B < \beta \leq \pi \end{cases} \tag{21}$$

Solving Eq. (21), we obtain the stable SGFD coefficients of the spatial first-order derivatives. The corresponding errors of the objective function are expressed as

$$\varepsilon(\beta) = \begin{cases} \varphi(\beta)/\beta - 1, \ 0 \leq \beta \leq B \\ \varphi(\beta)/\beta - f(\beta), \ B < \beta \leq \pi \end{cases} \tag{22}$$

One thing should be noticed that Eq. (21) is a piecewise function, which indicates that this function will become unsmooth when $\beta = B$. Therefore, a transition interval $[B, B+\Delta\beta]$ is introduced to avoid the great error caused by the unsmooth point $\beta = B$. Then the region of β is divided into three parts, i.e., $[0, B]$, $[B, B+\Delta\beta]$ and $[B+\Delta\beta, \pi]$. Consequently, Eq. (21) can be changed as

$$\begin{cases} |\varphi(\beta)/\beta - 1| \le \eta, \ 0 \le \beta \le B \\ |\varphi(\beta)/\beta - f(\beta)| \le b\eta, \ B + \Delta\beta \le \beta \le \pi \end{cases} \tag{23}$$

There exist three maximum values of $\varphi(\beta)$ and $\varepsilon(\beta)$ respectively in these three intervals. These three maximum values of $\varphi(\beta)$ can be written as

$$\psi_1 = \max_{0 \le \beta \le B} |\varphi(\beta)| \tag{24}$$

$$\psi_2 = \max_{B < \beta \le B+\Delta\beta} |\varphi(\beta)| \tag{25}$$

$$\psi_3 = \max_{B+\Delta\beta < \beta \le \pi} |\varphi(\beta)| \tag{26}$$

The maximum value of $\varphi(\beta)$ over the whole wavenumber region can be represented as

$$\psi = \max(\psi_1, \psi_2, \psi_3) \tag{27}$$

Correspondingly, three maximum values of the objective function errors $\varepsilon(\beta)$ in these three intervals are given by

$$\varepsilon_1 = \max_{0 \le \beta \le B} |\varepsilon(\beta)| \tag{28}$$

$$\varepsilon_2 = \max_{B < \beta \le B+\Delta\beta} |\varepsilon(\beta)| \tag{29}$$

$$\varepsilon_3 = \max_{B+\Delta\beta < \beta \le \pi} |\varepsilon(\beta)| \tag{30}$$

Considering the high spatial accuracy when using REA for modeling, we adopt the idea of the REA to solve Eq. (23) and summarize the detailed process to obtain the new stable SGFD coefficients as follows.

(1) Set the SGFD operator length M and the tentative order $M_t = 1$ for the given B and η.
(2) Set initial values of β_i. The exact formulas are expressed in the following:

$$\beta_i = iB/M_t, 1 \le i \le M_t \tag{31}$$

$$\beta_i = B_2 + (i - M_t)(\pi - B_2)/(M - M_t), \quad M_t + 1 \le i \le M + 1 \tag{32}$$

where, $B_2 = B + \Delta\beta$.

(3) Compute the SGFD coefficients by solving Eq. (23). It can be rewritten in the same format as the linear Eq. (13). The exact expression is written as follows:

$$A_{i,j} = \begin{cases} 2\sin[(j-0.5)\beta_i]/\beta_i, \ 1 \le j \le M \\ (-1)^{i+1}, j = M+1, \ 1 \le i \le M_t \\ (-1)^i, j = M+1, \ M_t < i \le M \end{cases} \tag{33}$$

$$d_i = \begin{cases} 1, \ 1 \le i \le M_t \\ f(\beta)/b, \ M_t < i \le M \end{cases} \tag{34}$$

To conveniently and efficiently obtain a set of SGFD coefficients, the Gauss elimination method is adopted to solve the linear equations.

(4) Calculate the corresponding approximation error of the objective function and confirm whether it is under the accuracy error threshold. If the SGFD coefficients can meet the conditions $\varepsilon_1 \le \eta$ and $\varepsilon_3 \le b\eta$, they satisfy the accuracy requirements.
(5) Update β_i and M_t. If the calculated SGFD coefficients dissatisfy the error criterion, set the extreme points of $\varepsilon(\beta)$ as the updated β_i and go to Step (3). If the total number of extreme points lacks or exceeds $M+1$, update M_t and go to Step (2).

From the aforementioned analyses, we introduce two new parameters $\Delta\beta$ and b in the new method. To figure out the influence of $\Delta\beta$ and b on the new method, we draw Figs. 3 and 4.

Fig. 3 displays the variation of $\varphi(\beta)$ and $\varepsilon(\beta)$ with β when fixed $M = 15$, $B = 1.0$ and $b = 3.0$ for different values of $\Delta\beta$. In Fig. 3a, as $\Delta\beta$ varying, ψ_2 and ψ_3 will change. Exactly, increasing $\Delta\beta$ will increase ψ_2, whereas decrease ψ_3. The values of $\varphi(\beta)$ show a state of fluctuation in the interval $[B+\Delta\beta, \pi]$, and the fluctuation range increases with the increase of β. In Fig. 3b, the increase of $\Delta\beta$ will decrease the values of ε_1 and ε_3 and increase the value of ε_2.

Fig. 4 depicts variations of $\varphi(\beta)$ and $\varepsilon(\beta)$ with β for different values of b which set $M = 15$, $B = 1.0$ and $\Delta\beta = 0.3$. In Fig. 4a, it can be concluded that ψ_2 and ψ_3 increase with the increase of b. In Fig. 4b, ε_1 decreases with the increase of b, and the variations of ε_2 and ε_3 are on the contrary.

Generally, we can adjust these two new parameters, $\Delta\beta$ and b, to obtain better SGFD coefficients. The specific steps to obtain the optimal values of $\Delta\beta$ and b are described as follows:

(1) Let $b = 1$.
(2) Set $\Delta\beta$ and carry out the process of computing FD coefficients. Iterate over the value of $\Delta\beta$ until $|\psi_3/\psi_2 - 1| < \eta$.
(3) Estimate whether the value of ε_1 is smaller than η. If satisfied, end the run; otherwise, add the value of b and go to Step (2).

2.4. Stability analysis for the new method

We introduce an appropriate function $f(\beta)$ to make the values of $\varphi(\beta)$ approach some given values outside the given wavenumber region. We hope that the values of $\varphi(\beta)$ approach β and B in the wavenumber intervals $[0, B]$ and $[B, \pi]$, respectively. Therefore, B is expected to become the maximum value that $\varphi(\beta)$ can reach in the whole interval $[0, \pi]$. Combined with Eq. (A-9) in Appendix A, we obtain the maximum value of $r_{\max}$ that can be writen as follows:

$$\lim r_{\max} = \sqrt{2}/B \tag{35}$$

It can be concluded that the value of $\lim r_{\max}$ varies with B. Therefore, if $B < 2$, $\lim r_{\max}$ in the new method will become bigger than that in the conventional SGFD method.

Fig. 5 illustrates variation of the maximum CFL number $r_{\max}$ with B for the conventional and the new methods. Under the same accuracy η and SGFD operator length M, values of $r_{\max}$ in the new method are significantly bigger than those in the conventional method, especially when B is smaller than 1.0, indicating that the stability of the new method is better than the conventional method.

For conciseness and clarity, in Table 1, we list the changes of $\Delta\beta$,

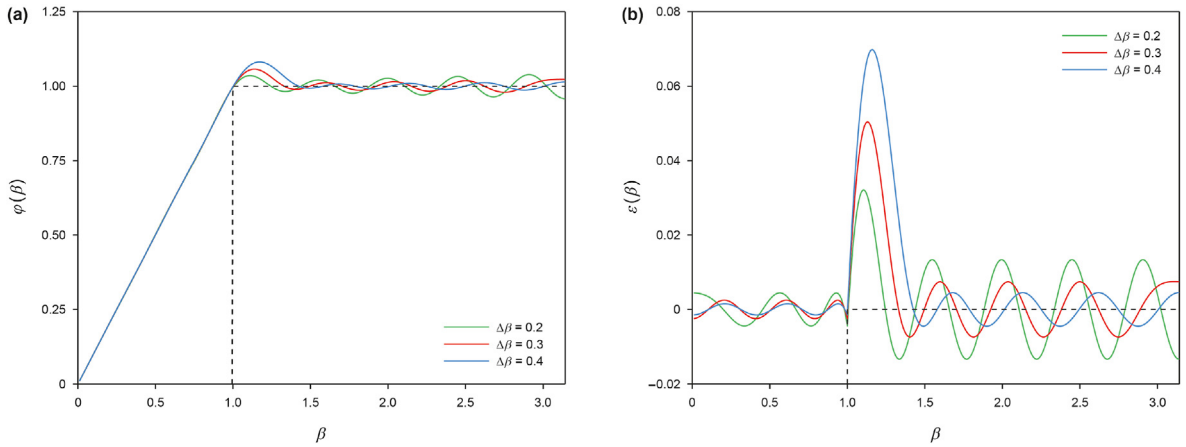

Fig. 3. Variations of (a) $\varphi(\beta)$ and (b) $\varepsilon(\beta)$ with β for different values of $\Delta\beta$. $M = 15$, $B = 1.0$, $b = 3.0$.

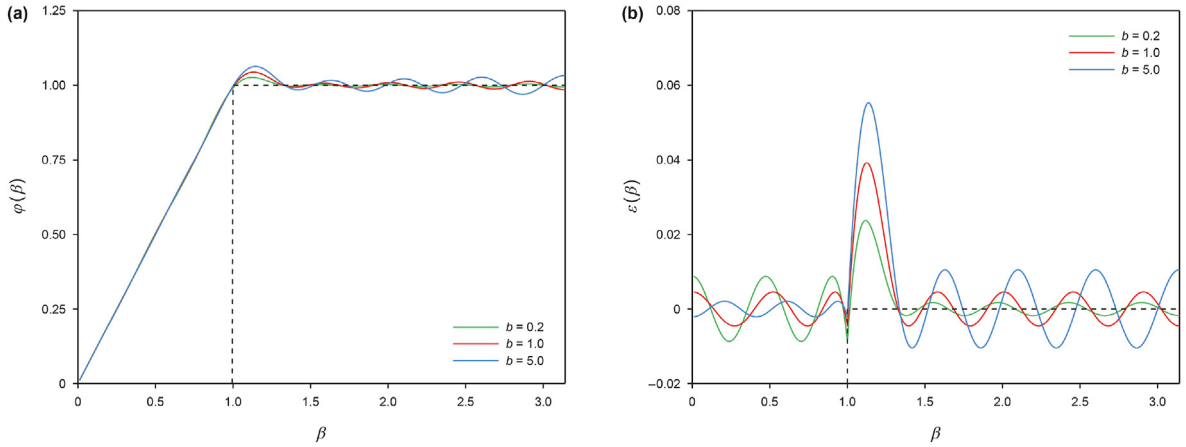

Fig. 4. Variations of (a) $\varphi(\beta)$ and (b) $\varepsilon(\beta)$ with β for different values of b. $M = 15$, $B = 1.0$, $\Delta\beta = 0.3$.

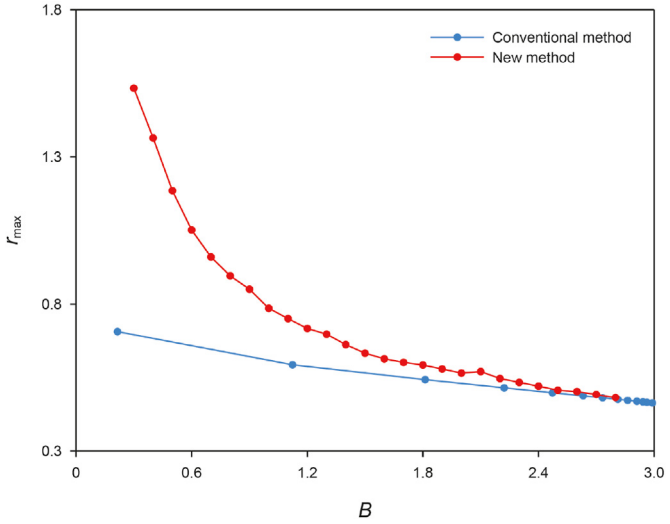

Fig. 5. The maximum CFL number r_{max} for the conventional and the new methods. $\eta = 1E-3$. For the conventional method, as M changes from 1 to 15, B ranges from 0.22 to 2.8 and r_{max} varies from 0.707 to 0.461. For the new method, $M = 15$, as B changes from 0.3 to 2.8, B varies from 1.534 to 0.482.

B and r_{max} with B when M is 15 and 30 respectively. These parameters can be used to calculate SGFD coefficients of the new method through Eq. (23), directly. In addition, it can be observed from Table 1 that in the case of fixed B, the value of r_{max} increases with the increase of M for the smaller wavenumber interval, while the value of r_{max} is almost similar when M is different for the bigger wavenumber interval.

In Table 2, we list the SGFD coefficients obtained by the new method when $M = 15$ and $\eta = 1E-3$, and these SGFD coefficients can be used for wavefield modeling. In order to model a situation where the maximum CFL number r_{max} is larger, the SGFD coefficients corresponding to a smaller B can be selected for modeling.

3. Examples

In this section, we employ the new method to simulate acoustic wave propagation and test its adaptation for two different velocity models, i.e., the homogeneous model and the Marmousi model. In all numerical modeling examples, we fix the spatial grid spacing $dx = dz = 5$ m and vary the maximum CFL number r_{max} to verify the effect of the new method.

3.1. Test on the homogeneous model

First, we implement numerical modeling without absorbing boundary conditions in a 2D homogeneous model whose

Table 1
Variations of $\Delta\beta$, b and r_{max} with B when $M = 15$ and $M = 30$. $\eta = 1E-3$.

B	$M = 15$				$M = 30$			
	$\Delta\beta$	b	r_{max} of 2D	r_{max} of 3D	$\Delta\beta$	b	r_{max} of 2D	r_{max} of 3D
0.3	0.38	48.5	1.5335	1.2521	0.21	27.0	1.7545	1.4326
0.4	0.43	50.9	1.3641	1.1138	0.46	27.3	1.4088	1.1502
0.5	0.35	34.1	1.1850	0.9675	0.21	24.3	1.2626	1.0309
0.6	0.33	43.6	1.0514	0.8584	0.16	15.8	1.1190	0.9136
0.7	0.32	38.0	0.9599	0.7837	0.15	13.8	1.0205	0.8332
0.8	0.30	32.4	0.8961	0.7316	0.14	10.7	0.9393	0.7670
0.9	0.29	26.3	0.8507	0.6946	0.14	15.4	0.8738	0.7135
1.0	0.29	27.4	0.7859	0.6417	0.13	10.4	0.8206	0.6700
1.1	0.26	30.1	0.7507	0.6130	0.13	15.6	0.7741	0.6321
1.2	0.27	33.1	0.7172	0.5856	0.12	10.5	0.7420	0.6058
1.3	0.28	26.7	0.6977	0.5696	0.11	9.8	0.7076	0.5777
1.4	0.26	25.9	0.6622	0.5407	0.29	9.4	0.6789	0.5543
1.5	0.24	23.8	0.6330	0.5168	0.29	8.8	0.6497	0.5305
1.6	0.23	26.3	0.6137	0.5011	0.10	8.6	0.6273	0.5122
1.7	0.22	25.2	0.6017	0.4913	0.10	7.9	0.6147	0.5019
1.8	0.23	26.1	0.5928	0.4840	0.10	11.8	0.6019	0.4914
1.9	0.23	27.2	0.5793	0.4730	0.09	7.7	0.5905	0.4822
2.0	0.24	73.3	0.5654	0.4616	0.09	7.7	0.5824	0.4755
2.1	0.20	24.1	0.5704	0.4657	0.09	8.0	0.5790	0.4727
2.2	0.19	28.2	0.5470	0.4466	0.39	13.2	0.5505	0.4495
2.3	0.21	26.7	0.5338	0.4358	0.10	10.3	0.5379	0.4392
2.4	0.20	21.0	0.5207	0.4252	0.32	18.2	0.5241	0.4280
2.5	0.20	86.6	0.5069	0.4139	0.33	22.0	0.5148	0.4204
2.6	0.16	15.0	0.5024	0.4102	0.15	16.7	0.5000	0.4082
2.7	0.15	12.8	0.4922	0.4019	0.31	17.2	0.4921	0.4018
2.8	0.49	100.5	0.4819	0.3934	0.08	19.7	0.4812	0.3929

horizontal and vertical distances are both 2 km.

The velocity of the model is 3000 m/s, and a Ricker wavelet with the dominant frequency of 25 Hz is excited in the center of the computational domain. We keep the spatial operator length M as 15 for both the conventional and the new methods. Specific modeling parameters are listed in the caption of Fig. 6. Fig. 6a and c shows results simulated by the conventional method whose temporal sampling intervals are $\tau = 0.5$ ms and $\tau = 1.0$ ms, i.e., $r = 0.3$ and 0.6 respectively. Fig. 6b, 6d–h is snapshots modeled by the new method, with SGFD coefficients are displayed in Table 2. Among them, in Fig. 6b, $\tau = 0.5$ ms, $r = 0.3$. In Fig. 6d–f, $\tau = 1.0$ ms, $r = 0.6$. In Fig. 6g–h, $\tau = 1.4$ ms, $r = 0.84$. It can be observed that waveforms are able to propagate normally when $\tau = 0.5$ ms in Fig. 6a. However, when $\tau = 1.0$ ms, compared to the waveform simulated using the new method in Fig. 6d and c cannot produce a normal waveform, and after propagating for a certain period, the wavefield value becomes infinite, making it impossible to obtain seismic records. Therefore, when $\tau \geq 1.0$ ms, we can no longer use the conventional method to perform stable modeling. By contrast, it remains stable by the new method when $\tau = 1.0$ ms and $\tau = 1.4$ ms in Fig. 6e and g, respectively. Furthermore, we plot stable snapshots at $\tau = 1.0$ ms and $\tau = 1.4$ ms when $t = 6000$ ms in Fig. 6f and h, respectively. It can be seen that, for the new method, the wavefield can still maintain waveform after a long-time propagation, indicating that the wavefield is stable.

Based on the theory that the energy of wavefield will maintain a constant when do not consider absorbing boundary conditions, we compute the root-mean-squared (RMS) amplitude A_{RMS} of the whole model in different propagation time and observe the variation of $\mathrm{Log}_{10}(A_{RMS})$ for the conventional and the new methods in Fig. 7a. One can observe that the variation trend of the RMS amplitude A_{RMS} in the conventional method is exponential, indicating that the modeling is unstable; whereas in the new method, the RMS amplitude remains in a steady state, manifesting that the modeling is stable. In Fig. 7b, it can be observed that the RMS amplitude simulated by the new method remains stable over long-time recording even with a larger CFL number, suggesting that the new method is available to model with a large time sampling interval and a long-time propagation.

Decreasing B or the dominant frequency, we can model with a larger maximum CFL number as exhibited in Fig. 8. The modeling parameters are illustrated in the caption of the figure. Fig. 8a displays a snapshot at $r = 1.50$ for the homogeneous model obtained by the new method. Corresponding spatial SGFD coefficients are demonstrated in Table 2. In Fig. 8a, the value of r_{max} for the new method achieves more than twice as much as the conventional method. We use the SGFD coefficients listed in Table 3 to obtain Fig. 8b, showing a snapshot that reaches a much larger maximum CFL number $r = 1.75$. All of these figures demonstrate the stability of the new method.

Notice that, though we can adopt optimal SGFD methods calculating SGFD coefficients to reduce spatial dispersion, temporal accuracy is still second order and thus high time dispersion will generate when modeling with a large time sampling interval. It can be observed that time dispersion in Fig. 6e and g is more serious compared with Fig. 6a and b. In Fig. 9, we plot an extracted synthesized seismogram for the homogeneous model whose modeling parameters are similar to that in Fig. 6g and h, as shown by the blue curves. Compared with the analytic solutions, the blue curve occurs manifestly time dispersion problem. Therefore, the time-dispersion correction is adopted to suppress the time dispersion. We apply the forward time dispersion transform (FTDT) (Koene et al., 2018; Liu, 2020a) to the Ricker wavelet as the source term and conduct the wave equation modeling as usual. After obtaining the synthesized seismogram, adopted the inverse time dispersion transform (ITDT)

Table 2
SGFD coefficients of the new method when $M = 15$ and $\eta = 1E-3$.

c_m	$B = 0.3$	$B = 0.4$	$B = 0.5$	$B = 0.6$	$B = 0.7$	$B = 0.8$
c_1	1.9249E-01	2.6625E-01	3.1776E-01	3.7908E-01	4.3915E-01	4.9826E-01
c_2	6.8349E-02	7.9604E-02	1.0285E-01	1.1711E-01	1.2913E-01	1.3754E-01
c_3	4.3585E-02	6.3015E-02	5.6075E-02	5.7496E-02	5.5256E-02	4.9972E-02
c_4	3.2018E-02	2.6825E-02	3.0538E-02	2.5220E-02	1.7542E-02	7.8498E-03
c_5	2.2232E-02	2.6077E-02	1.3071E-02	4.8179E-03	−4.5091E-03	−1.2003E-02
c_6	1.4300E-02	4.2355E-04	−1.5772E-04	−7.6170E-03	−1.2528E-02	−1.4330E-02
c_7	5.9751E-03	1.0072E-03	−6.8994E-03	−1.0904E-02	−1.1482E-02	−7.5482E-03
c_8	7.0683E-04	−1.1136E-02	−9.6259E-03	−8.9410E-03	−3.6290E-03	2.2894E-03
c_9	−4.4519E-03	−6.5999E-03	−6.5533E-03	−2.4339E-03	2.1371E-03	6.3181E-03
c_{10}	−4.6592E-03	−6.0364E-03	−4.1703E-03	1.6225E-03	7.2722E-03	6.5627E-03
c_{11}	−7.5650E-03	−2.0937E-03	1.8579E-03	6.2690E-03	4.2071E-03	1.1774E-04
c_{12}	−3.0344E-03	3.0886E-03	−1.2514E-05	3.3666E-03	9.3957E-03	−1.3189E-03
c_{13}	−1.9152E-02	−1.3193E-03	2.3697E-02	1.2617E-02	−2.6046E-02	−1.8734E-02
c_{14}	3.2539E-02	1.5378E-02	−2.0067E-02	−2.5169E-02	1.3339E-02	2.0380E-02
c_{15}	−1.0044E-02	−9.5199E-03	3.3798E-03	9.8871E-03	−1.0551E-03	−5.9119E-03

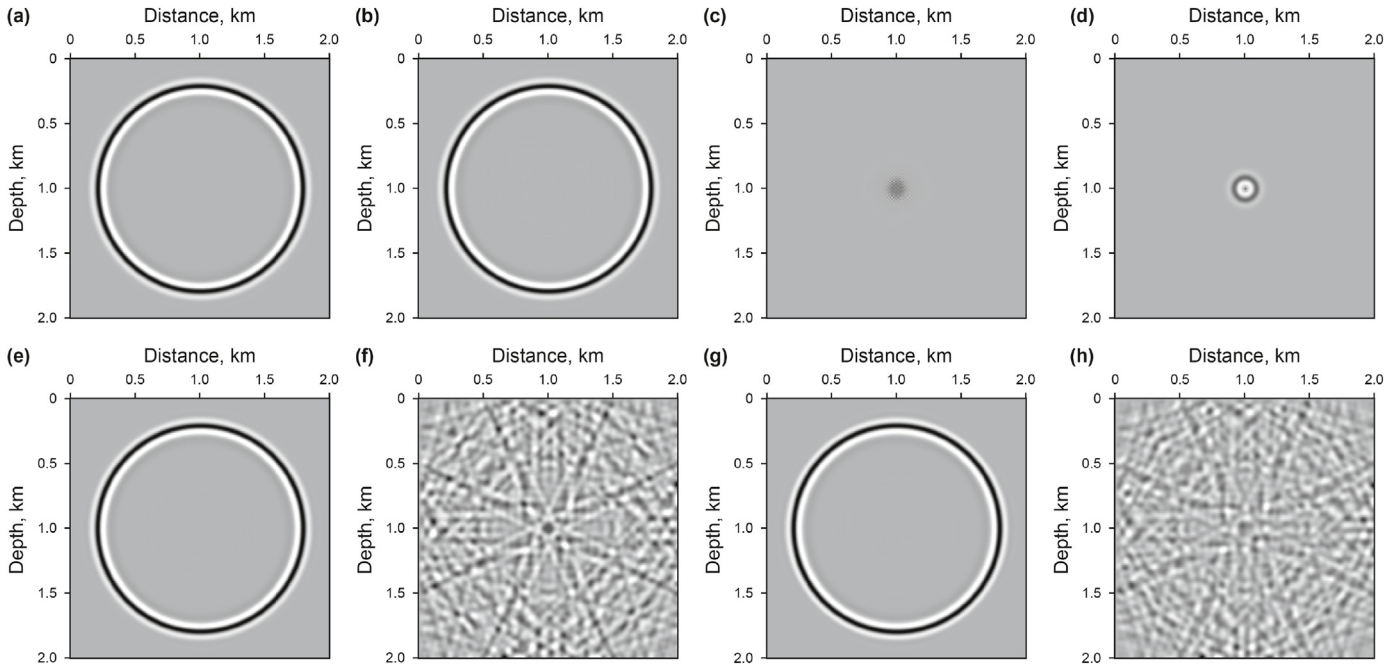

Fig. 6. Snapshots computed by the conventional and the new methods for the homogeneous model without ABC whose velocity, size, grid intervals and dominant frequency are 3000 m/s, 2000 m × 2000 m, 5 m, and 25 Hz respectively. The spatial SGFD operator length M is 15. $\eta = 1E-3$. For the conventional method, (a) $\tau = 0.5$ ms, $t = 300$ ms. (c) $\tau = 1.0$ ms, $t = 65$ ms. For the new method, $B = 0.8$, (b) $\tau = 0.5$ ms, $t = 300$ ms. (d) $\tau = 1.0$ ms, $t = 65$ ms. (e) $\tau = 1.0$ ms, $t = 300$ ms. (f) $\tau = 1.0$ ms, $t = 6000$ ms. (g)–(h) $\tau = 1.4$ ms, $t = 300$ ms and 6000 ms respectively. The conventional method is unstable while the new method still maintain stable when $\tau \geq 1$ ms.

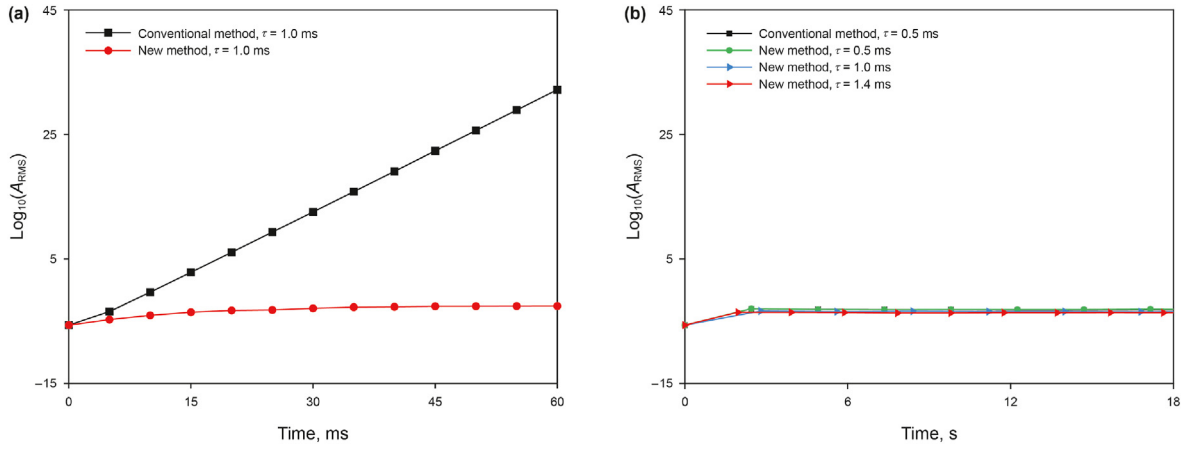

Fig. 7. Variations of $\mathrm{Log}_{10}(A_{\mathrm{RMS}})$ with propagation time for the conventional and new methods. (a) $\tau = 1.0$ ms. (b) $\tau = 0.5$ ms for the conventional method and $\tau = 0.5$ ms, 1.0 ms and 1.4 ms for the new method.

(Koene et al., 2018; Liu, 2020a) to it and then the high temporal accuracy synthesized seismogram will be obtained. It appears that the synthesized seismogram with time-dispersion correction in the red dot almost coincides with the reference solution in Fig. 9, indicating that the time-dispersion correction has a good performance in removing temporal dispersion when applied in our new method.

Table 4 displays the central processing unit (CPU) times for generating Fig. 6 using conventional and new methods, with a maximum recorded wave propagation time of 6 s. One can see that the CPU time decreases with the increase of the time step.

3.2. Test on the Marmousi model

The second example is a 2D complex model.

In Fig. 10, part of the velocity profile of the 2D Marmousi model with the horizontal and vertical sizes of 2500 m and 1750 m, respectively, is displayed. The source term used here is a 15 Hz Ricker wavelet, and we place the source at the position of (1250 m, 50 m). The locations of the receivers range from 0 m to 2500 m with an interval of 5 m at a depth of 5 m. The velocity varies from 1500 m/s to 4700 m/s and the operator length M is 15. According to Eq. (16), for the conventional method, when set $M = 15$, $r_{\max} = 0.461$, which means that the modeling will become unstable when $r > 0.461$. Fig. 11 displays the snapshots and seismograms obtained by the new method with a reference solution obtained by the conventional method using a very small time sampling interval 0.01 ms. Table 3 lists the specific SGFD coefficients used in Fig. 11. One should be noticed that the time interval τ in Fig. 11 is 0.8 ms, and thus the CFL number r varies from 0.240 to 0.752, which is

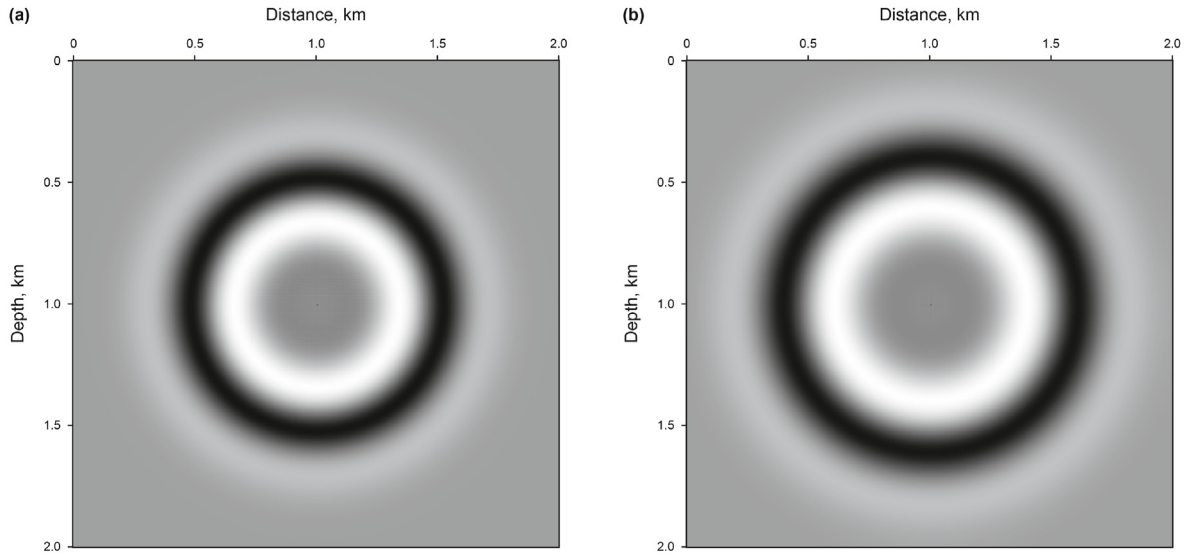

Fig. 8. Snapshots computed by the new method for the homogeneous model whose size, grid intervals and dominant frequency are 2000 m × 2000 m, 5 m and 6 Hz respectively. $B = 0.3$ and $\eta = 1E-3$. (a) $v = 3000$ m/s, $M = 15$, $\tau = 2.5$ ms, $r = 1.5$, $t = 325$ ms. (b) $v = 3500$ m/s, $M = 30$, $\tau = 2.5$ ms, $r = 1.75$, $t = 325$ ms. The new method is able to model with a much larger CFL number.

Table 3
FD coefficients of the new method when $M = 15$ for $B = 1.0$ and $M = 30$ for $B = 0.3$. $\eta = 1E-3$.

c_m	$M = 15$	$M = 30$	c_m	$M = 15$	$M = 30$	c_m	$M = 30$
c_1	6.1330E-01	1.9270E-01	c_{11}	−4.9559E-03	−4.9786E-04	c_{21}	2.1498E-03
c_2	1.4597E-01	6.1064E-02	c_{12}	−5.1887E-03	−4.3770E-03	c_{22}	4.3858E-04
c_3	3.1997E-02	3.8739E-02	c_{13}	1.9162E-02	−1.8088E-03	c_{23}	1.4851E-03
c_4	−1.3021E-02	2.3140E-02	c_{14}	−1.3449E-02	−4.2404E-03	c_{24}	−1.4721E-04
c_5	−1.9575E-02	1.9584E-02	c_{15}	2.8432E-03	−1.0404E-03	c_{25}	5.2724E-04
c_6	−7.6399E-03	1.0647E-02	c_{16}		−2.5606E-03	c_{26}	−4.9842E-04
c_7	6.0218E-03	9.9611E-03	c_{17}		6.1330E-04	c_{27}	−3.6209E-04
c_8	8.4570E-03	2.9774E-03	c_{18}		−6.6120E-04	c_{28}	9.1779E-04
c_9	3.1913E-03	3.4464E-03	c_{19}		1.9015E-03	c_{29}	−8.2010E-03
c_{10}	−5.0091E-03	−2.0364E-03	c_{20}		4.2656E-04	c_{30}	5.8744E-03

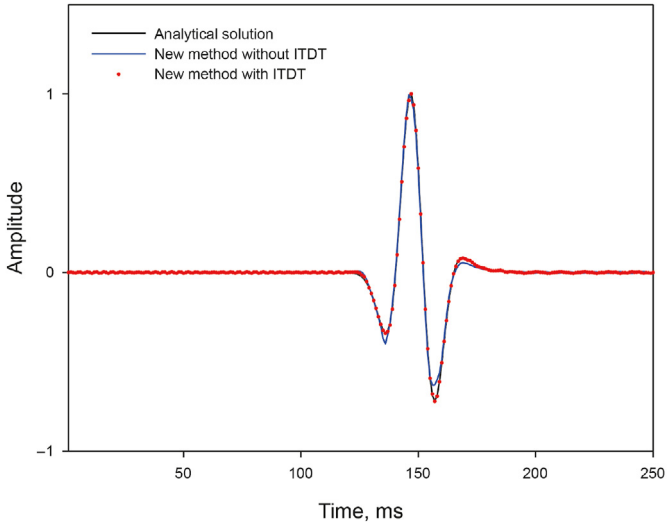

Fig. 9. Waveforms at (505 m, 5 m) of the homogeneous model. The black solid line is the analytical solution. The blue solid line and the red dashed line are the waveforms without and with ITDT obtained by the new method, respectively. The parameters of modeling in the new method are the same as those in Fig. 6e and f.

Table 4
Comparison of computational costs for conventional and new methods.

Method	Conventional	New	New	New
Time sampling interval, ms	0.5	0.5	1.0	1.4
Courant number	0.3	0.3	0.6	0.84
CPU time, s	647.382	653.422	354.266	261.567

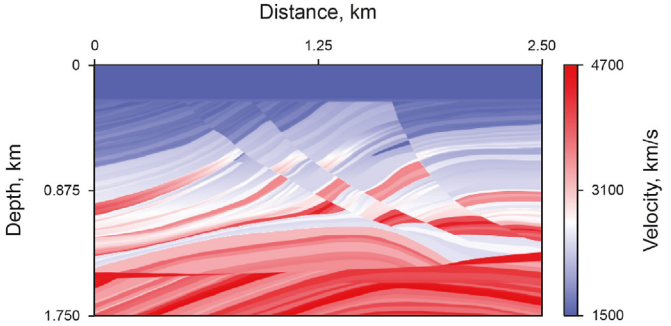

Fig. 10. The velocity profile of the Marmousi model.

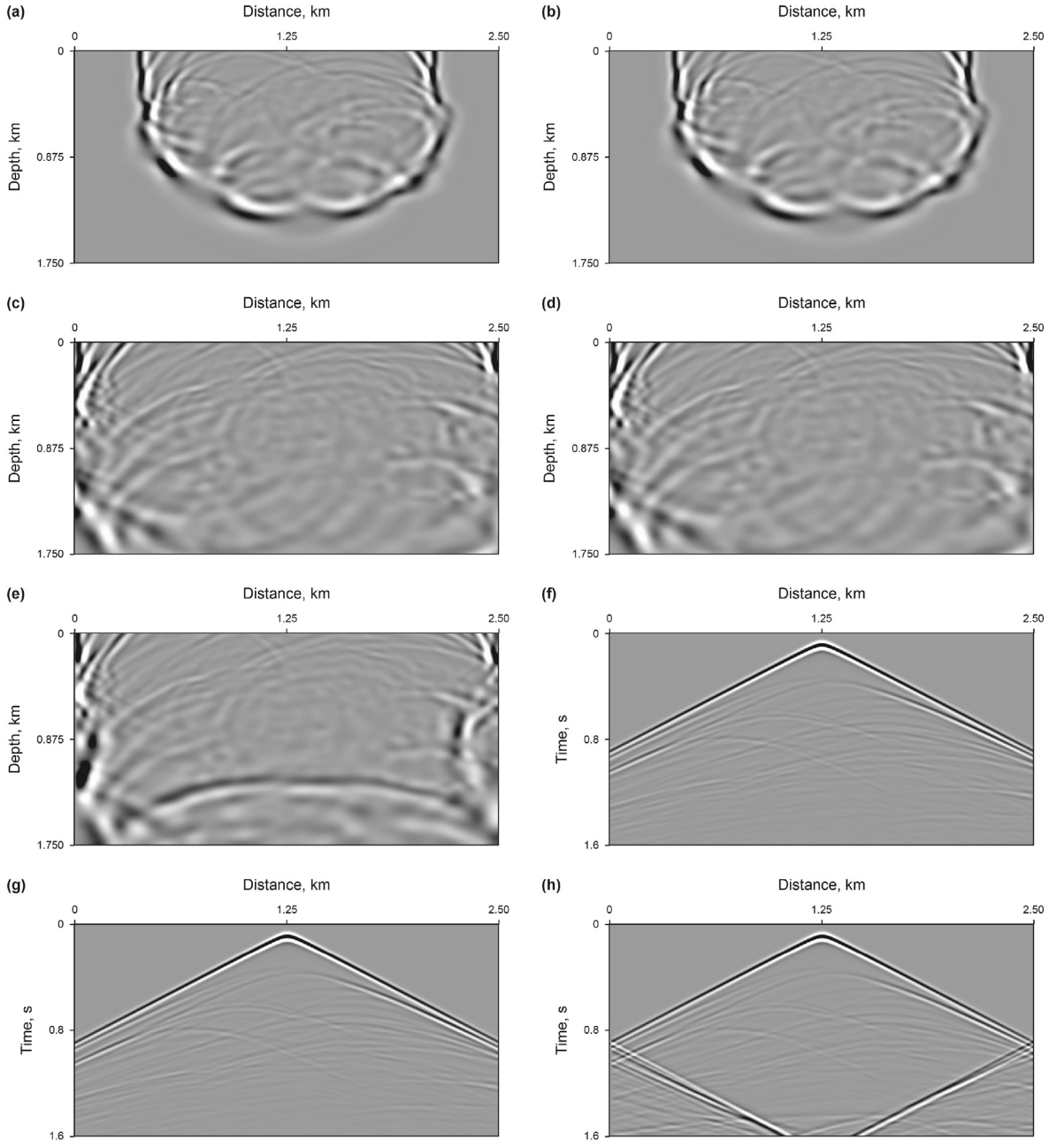

Fig. 11. Snapshots and seismograms for the Marmousi model with and without HABC computed by the new methods. $v = 1500–4700$ m/s, $h = 5$ m, $\tau = 0.8$ ms, $f = 15$ Hz, $M = 15$, $D = 15$ and $B = 1.0$. Thus $r = 0.240–0.752$. (a) Reference snapshot at $t = 0.64$ s. (b) The snapshot at $t = 0.64$ s. (c) Reference snapshot at $t = 0.88$ s with HABC. (d) The snapshot at $t = 0.88$ s with HABC. (e) The snapshot at $t = 0.88$ s without HABC. (f) Reference seismogram with HABC. (g) The seismogram with HABC. (h) The seismogram without HABC.

higher than the maximum CFL number achievable by the conventional method. The conventional method cannot be used to model with these parameters, but the new method yields good results as shown in Fig. 11g–h, where the seismograms display good stability and are close to the reference solution when $r > 0.461$.

We use an HABC (Liu and Sen, 2010, 2018) that combines one-way wave equation (OWWE) (Clayton and Engquist, 1977; Higdon, 1991) and the two-way wave equation (TWWE) in the boundary to absorb artificial reflections at the model boundary. The computational area is divided into three parts: the inner area, the transition area, and the boundary area. The total thickness of the transition and boundary areas is denoted as D, with the thickness of the boundary area being one node. We test the linear weighting coefficient (Liu and Sen, 2010), the exponential weighting coefficient (Liu and Sen, 2018) and the parabolic weighting coefficient, respectively. The modeling results show that the parabolic weighting coefficient $\omega_i = \left(\frac{i-1}{D}\right)^2 + 2\left(\frac{i-1}{D}\right), (1 \le i \le D)$ has the best performance in removing the boundary reflection in the new method. As D increases, the absorption effect of the HABC increases, but so does the computational cost. To balance the requirements of absorption effectiveness and computational efficiency, we set D equal the length of the FD operator M. Alternatively, if D is smaller than M, we need to use symmetric boundary conditions to solve the wave equation (Liu and Sen, 2010; Chang and Liu, 2013). The comparison between snapshots with and without HABC in Fig. 11d–e indicates that HABC has excellent absorbing capabilities.

The same conclusion can be drawn from the comparison of seismograms with and without HABC in Fig. 11g–h.

Fig. 12 extracts single traces from Fig. 11 to compare waveforms. Fig. 12a shows the waveforms at (1250 m, 5 m). The blue dashed line and the red solid line represent the waveforms without and with ITDT, respectively. It can be seen that after applying ITDT, the waveform is closer to the reference solution. In addition, in Fig. 12b, we extract single traces from synthesized seismograms with different time sampling intervals at (1015 m, 5 m) to make a clearer comparison. Trace 1 is the waveform obtained by the conventional method with $\tau = 0.4$ ms. Traces 2 and 3 are the waveforms obtained by the new method with time sampling intervals of $\tau = 0.4$ ms and 0.8 ms, where the variations of the maximum CFL numbers are 0.120–0.376 and 0.240–0.752, respectively. When $\tau = 0.8$ ms, the conventional method is no longer able to maintain modeling stability, while the seismogram waveforms obtained by the new method can match the reference trace almost perfectly, demonstrating that the new method maintains high accuracy and stability simultaneously. Furthermore, the value of r can be further increased by increasing the SGFD operator length and decreasing the dominant frequency and B. Therefore, in Fig. 12c, we perform modeling with larger time sampling intervals, and the corresponding single traces extracted from the synthesized seismograms are displayed. In Fig. 12c, trace 1 is the waveform obtained by the conventional method with $\tau = 0.4$ ms. Traces 2 and 3 have time sampling intervals of 0.4 ms and 1.8 ms, where the variations of the maximum CFL numbers are 0.120–0.376 and 0.540–1.692, respectively. Fig. 12c also shows great modeling effect and has the same conclusions as Fig. 12b.

4. Discussion

In this section, we discuss the stability and potential applications of the new method in the 3D case.

For the conventional method, the CFL number in 3D case should satisfy the following condition (Liu and Sen, 2011):

$$r \le r_{\max} = \left(\sqrt{3} \sum_{m=1}^{M} |c_m| \right)^{-1} \tag{36}$$

Therefore, we calculate the variation of $r_{\max}$ with B in the 3D case, and the results are shown in Table 1. According to Eq. (A-9) in Appendix A, the maximum value of $r_{\max}$ in 3D case is:

$$\lim r_{\max} = 2 \Big/ \left(\sqrt{3} B \right) \tag{37}$$

During the process of wavefield modeling, the stability of conventional method is affected when the spatial sampling interval is

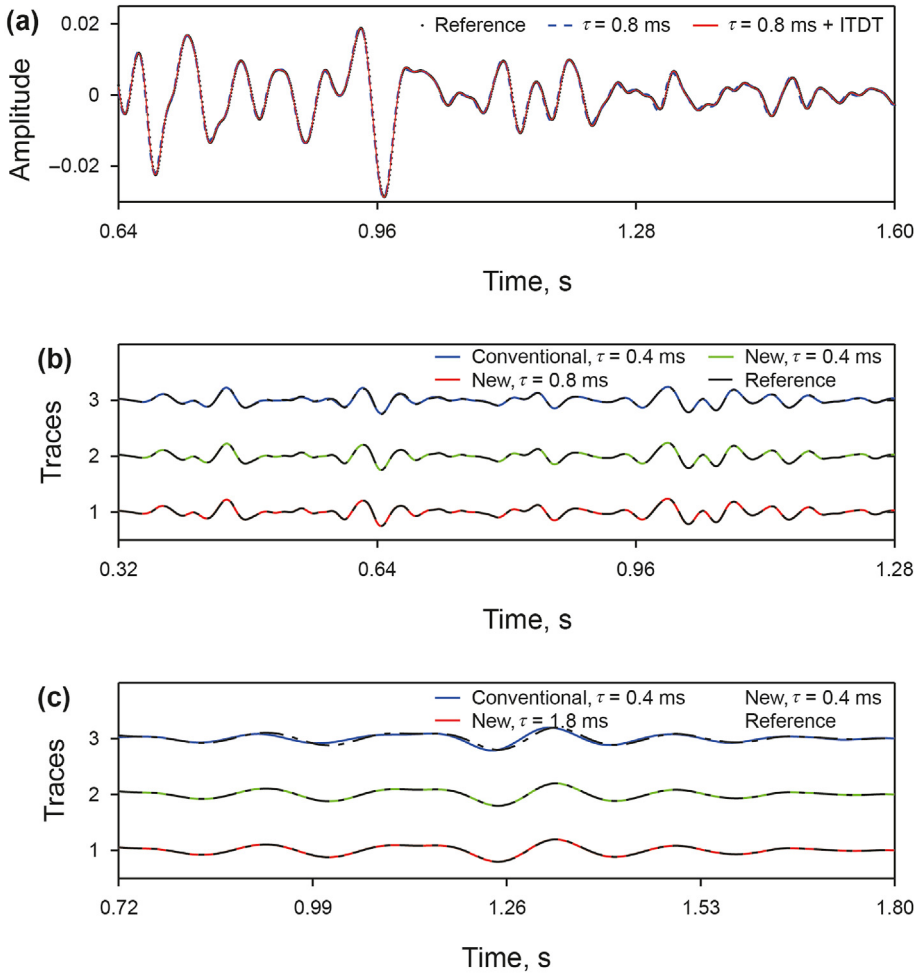

Fig. 12. Waveforms of the Marmousi model. v = 1500–4700 m/s, $h = 5$ m. The reference solutions are computed by the conventional SGFD method with $\tau = 0.01$ ms. (a) Waveforms comparison at (1250 m, 5 m) obtained by the new method without and with ITDT. (b) and (c) are the waveforms comparison at (1015 m, 5 m) with different time sampling intervals. For (a) and (b), $f = 15$ Hz, $M = 15$, $D = 15$ and $B = 1.0$. For (c), $f = 4$ Hz, $M = 30$, $D = 30$ and $B = 0.3$.

small, the time sampling interval is large, or the velocity is high. Typically, increasing the spatial sampling interval and reducing the time sampling interval are done to ensure that the modeling can proceed normally. However, this will increase the computational load, especially in 3D case. The new method overcomes the limit of the maximum CFL number of conventional method and can use larger CFL numbers for modeling while ensuring accuracy. It has great application prospects in 3D modeling.

In the days to come, we will develop the idea of the new method into the time-space domain SGFD method. By approximating the time-space domain dispersion relation, we aim to improve simulation accuracy and break stability limits simultaneously, thereby avoiding the additional computational cost associated with time-dispersion correction strategy.

5. Conclusions

We develop a new SGFD scheme to compute the spatial first-order FD coefficients for the acoustic wave equation. The basic idea is to rebuild the objective function which lets the spatial SGFD dispersion approximate the given values over the whole wavenumber area, leading to maximizing the CFL number and improving the stability of the modeling. Theoretical derivation and dispersion analysis show the advantages of our scheme. Compared with the conventional SGFD scheme, our scheme easily breaks up the limitation of conventional stability, making it capable of modeling with large CFL numbers, larger time sampling intervals, or smaller space sampling intervals while maintaining modeling accuracy. In addition, the HABC can be well combined with the proposed scheme to absorb the reflection from the boundary when appropriate weighting coefficients are chosen.

Conflict of interest statement

We declare that we have no financial and personal relationships with other people or organizations that can inappropriately influence our work, there is no professional or other personal interest of any nature or kind in any product, service and/or company that could be construed as influencing the position presented in, or the review of, the manuscript entitled “A Stable Staggered-Grid Finite-Difference Scheme for Acoustic Modeling beyond Conventional Stability Limit”.

Acknowledgments

This research is supported by the National Natural Science Foundation of China (NSFC) under contract no. 42274147.

Appendix A

In this part, we deduce the 2D stability condition for the conventional SGFD method (Liu and Sen, 2011).

Based on the von Neumann stability analysis, we define

$$q_{j,l}^{0} = p_{j,l}^{-1} \tag{A-1}$$

$$\mathbf{U}_{j,l}^{0} = \left(p_{j,l}^{0}, q_{j,l}^{0}\right)^{\mathrm{T}} = \mathbf{W}^{0} \mathrm{e}^{\mathrm{i}(j\beta_x + l\beta_z)} \tag{A-2}$$

where,

$$\mathbf{W}^{n} = \left(\mathrm{e}^{-\mathrm{i}\omega(t+n\tau)}, \mathrm{e}^{-\mathrm{i}\omega(t+(n-1)\tau)}\right) \tag{A-3}$$

Substituting Eq. (A-1), Eq. (A-2), and Eq. (A-3) into the recursive Eq. (6), we acquire

$$\mathbf{W}^{1} = \mathbf{G}\mathbf{W}^{0} = \begin{bmatrix} g & -1 \\ 1 & 0 \end{bmatrix} \mathbf{W}^{0} \tag{A-4}$$

where **G** is a transition matrix,

$$g = 2 - r^2\left[\varphi^2(\beta_x) + \varphi^2(\beta_z)\right] \tag{A-5}$$

To make the recursion Eq. (6) stable, the absolute values of transition matrix eigenvalues should be less than or equal 1 (Liu, 2020b, 2022). Therefore, we set

$$|g| \le 2 \tag{A-6}$$

Then, the roots of the eigenvalue equation $\lambda^2 - g\lambda + 1 = 0$ will be less than or equal 1.

Next, substituting Eq. (A-5) into Eq. (A-6), we can obtain the following inequality:

$$0 \le \left| r^2\left[\varphi^2(\beta_x) + \varphi^2(\beta_z)\right] \right| \le 4 \tag{A-7}$$

It can be deduced that the FD dispersion relations $\varphi(\beta_x)$ and $\varphi(\beta_z)$ play important roles to maintain the stability of modeling. According to Liu (2020b), we simplify Eq. (A-7) and obtain the exact relation of the stability. Let

$$\psi = \max_{0 \le x \le \pi} \varphi(x) \tag{A-8}$$

Then, Eq. (A-8) can be simplified as:

$$r \le r_{\max} = \sqrt{2} \Big/ \psi \tag{A-9}$$

which means the modeling will be stable when the CFL number is smaller than the maximum CFL number $r_{\max}$ and Eq. (A-9) is also called the stability condition. It can be concluded that $r_{\max}$ depends on ψ, i.e., the maximum value of the spatial FD dispersion.

References

Alford, R., Kelly, K., Boore, D.M., 1974. Accuracy of finite-difference modeling of the acoustic wave equation. Geophysics 39, 834–842. https://doi.org/10.1190/1.1440470.

Amundsen, L., Pedersen, Ø., 2017. Time step n-tupling for wave equations. Geophysics 82, T249–T254. https://doi.org/10.1190/geo2017-0377.1.

Bansal, R., Sen, M.K., 2008. Finite-difference modelling of S-wave splitting in anisotropic media. Geophys. Prospect. 56, 293–312. https://doi.org/10.1111/j.1365-2478.2007.00693.x.

Baysal, E., Kosloff, D.D., Sherwood, J.W., 1983. Reverse time migration. Geophysics 48, 1514–1524. https://doi.org/10.1190/1.1441434.

Chang, S.L., Liu, Y., 2013. A truncated implicit high-order finite-difference scheme combined with boundary conditions. Appl. Geophys. 10, 53–62. https://doi.org/10.1007/s11770-012-0342-4.

Chen, H., Zhou, H., Zhang, Q., et al., 2016a. Modeling elastic wave propagation us ing k-space operator-based temporal high-order staggered-grid finite-difference method. IEEE Trans. Geosci. Rem. Sens. 55, 801–815. https://doi.org/10.1109/TGRS.2016.2615330.

Chen, H., Zhou, H., Zhang, Q., et al., 2016b. A k-space operator-based least-squares staggered-grid finite-difference method for modeling scalar wave propagation. Geophysics 81, T45–T61. https://doi.org/10.1190/geo2015-0090.1.

Chen, J.B., 2007. High-order time discretizations in seismic modeling. Geophysics 72, SM115–SM122. https://doi.org/10.1190/1.2750424.

Chen, Y., Yang, G., Ma, X., et al., 2016c. A time–space domain stereo finite difference method for 3D scalar wave propagation. Comput. Geosci.-UK. 96, 218–235. https://doi.org/10.1016/j.cageo.2016.08.009.

Clayton, R., Engquist, B., 1977. Absorbing boundary conditions for acoustic and elastic wave equations. Bull. Seismol. Soc. Am. 67, 1529–1540. https://doi.org/10.1785/BSSA0670061529.

Dablain, M., 1986. The application of high-order differencing to the scalar wave equation. Geophysics 51, 54–66. https://doi.org/10.1190/1.1442040.

Etgen, J., Gray, S.H., Zhang, Y., 2009. An overview of depth imaging in exploration geophysics. Geophysics 74,. https://doi.org/10.1190/1.3223188. WCA5–WCA17.

Feng, Z., Schuster, G.T., 2017. Elastic least-squares reverse time migration. Geophysics 82, S143–S157. https://doi.org/10.1190/geo2016-0254.1.
Finkelstein, B., Kastner, R., 2008. A comprehensive new methodology for formulating FDTD schemes with controlled order of accuracy and dispersion. IEEE Trans. Antenn. Propag. 56, 3516–3525. https://doi.org/10.1109/TAP.2008.2005458.
Fornberg, B., 1988. Generation of finite difference formulas on arbitrarily spaced grids. Math. Comput. 51, 699–706. https://doi.org/10.1090/S0025-5718-1988-0935077-0.
Gaffar, M., Jiao, D., 2014. An explicit and unconditionally stable FDTD method for electromagnetic analysis. IEEE T. Microw. Theory. 62, 2538–2550. https://doi.org/10.1109/TMTT.2014.2358557.
Gaffar, M., Jiao, D., 2015. Alternative method for making explicit FDTD unconditionally stable. IEEE T. Microw. Theory. 63, 4215–4224. https://doi.org/10.1109/TMTT.2015.2496255.
Gao, Y., Zhang, J., Yao, Z., 2018. Removing the stability limit of the explicit finite-difference scheme with eigenvalue perturbation. Geophysics 83,. https://doi.org/10.1190/geo2018-0447.1. A93–A98.
Gao, Y., Zhang, J., Yao, Z., 2019. Extending the stability limit of explicit scheme with spatial filtering for solving wave equations. J. Comput. Phys. 397, 108853. https://doi.org/10.1016/j.jcp.2019.07.051.
He, Z., Zhang, J., Yao, Z., 2019. Determining the optimal coefficients of the explicit finite-difference scheme using the Remez exchange algorithm. Geophysics 84, S137–S147. https://doi.org/10.1190/geo2018-0446.1.
Higdon, R.L., 1991. Absorbing boundary conditions for elastic waves. Geophysics 56, 231–241. https://doi.org/10.1190/1.1443035.
Holberg, O., 1987. Computational aspects of the choice of operator and sampling interval for numerical differentiation in large-scale simulation of wave phenomena. Geophys. Prospect. 35, 629–655. https://doi.org/10.1111/j.1365-2478.1987.tb00841.x.
Jing, H., Chen, Y., Yang, D., et al., 2017. Dispersion-relation preserving stereo-modeling method beyond Nyquist frequency for acoustic wave equation. Geophysics 82, T1–T15. https://doi.org/10.1190/geo2016-0104.1.
Kelly, K.R., Ward, R.W., Treitel, S., et al., 1976. Synthetic seismograms: a finite-difference approach. Geophysics 41, 2–27. https://doi.org/10.1190/1.1440605.
Kindelan, M., Kamel, A., Sguazzero, P., 1990. On the construction and efficiency of staggered numerical differentiators for the wave equation. Geophysics 55, 107–110. https://doi.org/10.1190/1.1442763.
Koene, E.F., Robertsson, J.O., Broggini, F., et al., 2018. Eliminating time dispersion from seismic wave modeling. Geophys. J. Int. 213, 169–180. https://doi.org/10.1093/gji/ggx563.
Kosloff, D., Pestana, R.C., Tal-Ezer, H., 2010. Acoustic and elastic numerical wave simulations by recursive spatial derivative operators. Geophysics 75, T167–T174. https://doi.org/10.1190/1.3485217.
Levander, A.R., 1988. Fourth-order finite-difference P-SV seismograms. Geophysics 1425–1436. https://doi.org/10.1190/1.1442422.
Liu, H., Dai, N., Niu, F., et al., 2014. An explicit time evolution method for acoustic wave propagation. Geophysics 79, T117–T124. https://doi.org/10.1190/geo2013-0073.1.
Liu, Y., 2013. Globally optimal finite-difference schemes based on least squares. Geophysics 78, T113–T132. https://doi.org/10.1190/geo2012-0480.1.
Liu, Y., 2014. Optimal staggered-grid finite-difference schemes based on least-squares for wave equation modelling. Geophys. J. Int. 197, 1033–1047. https://doi.org/10.1093/gji/ggu032.
Liu, Y., 2020a. Acoustic and elastic finite-difference modeling by optimal variable-length spatial operators variable-length spatial finite difference. Geophysics 85, T57–T70. https://doi.org/10.1190/geo2019-0145.1.
Liu, Y., 2020b. Maximizing the CFL number of stable time–space domain explicit finite-difference modeling. J. Comput. Phys. 416, 109501. https://doi.org/10.1016/j.jcp.2020.109501.
Liu, Y., 2022. Removing the stability limit of the time–space domain explicit finite-difference schemes for acoustic modeling with stability condition-based spatial operators. Geophysics 87, T205–T223. https://doi.org/10.1190/geo2021-0141.1.
Liu, Y., Sen, M.K., 2009. A new time–space domain high-order finite-difference method for the acoustic wave equation. J. Comput. Phys. 228, 8779–8806. https://doi.org/10.1016/j.jcp.2009.08.027.
Liu, Y., Sen, M.K., 2010. A hybrid scheme for absorbing edge reflections in numerical modeling of wave propagation. Geophysics 75, A1–A6. https://doi.org/10.1190/1.3295447.
Liu, Y., Sen, M.K., 2011. Scalar wave equation modeling with time–space domain dispersion-relation-based staggered-grid finite-difference schemes. Bull. Seismol. Soc. Am. 101, 141–159. https://doi.org/10.1785/0120100041.
Liu, Y., Sen, M.K., 2013. Time–space domain dispersion-relation-based finite-difference method with arbitrary even-order accuracy for the 2D acoustic wave equation. J. Comput. Phys. 232, 327–345. https://doi.org/10.1016/j.jcp.2012.08.025.
Liu, Y., Sen, M.K., 2018. An improved hybrid absorbing boundary condition for wave equation modeling. J. Geophys. Eng. 15, 2602–2613. https://doi.org/10.1088/1742-2140/aadd31.
Long, G., Zhao, Y., Zou, J., 2013. A temporal fourth-order scheme for the first-order acoustic wave equations. Geophys. J. Int. 194, 1473–1485. https://doi.org/10.1093/gji/ggt168.
Ma, X., Yang, D., 2017. A phase-preserving and low-dispersive symplectic partitioned Runge–Kutta method for solving seismic wave equations. Geophys. J. Int. 209, 1534–1557. https://doi.org/10.1093/gji/ggx097.
McMechan, G.A., 1983. Migration by extrapolation of time-dependent boundary values. Geophys. Prospect. 31, 413–420. https://doi.org/10.1111/j.1365-2478.1983.tb01060.x.
Ren, Z., Dai, X., Bao, Q., et al., 2021. Time and space dispersion in finite difference and its influence on reverse time migration and full-waveform inversion. Chin. J. Geophys. 64, 4166–4180. https://doi.org/10.6038/cjg2021P0041 (in Chinese).
Ren, Z., Li, Z., 2017. Temporal high-order staggered-grid finite-difference schemes for elastic wave propagation temporal high-order SFD schemes. Geophysics 82, T207–T224. https://doi.org/10.1190/geo2017-0005.1.
Ren, Z., Liu, Y., 2015. Acoustic and elastic modeling by optimal time–pace domain staggered-grid finite-difference schemes optimal staggered-grid finite difference. Geophysics 80, T17–T40. https://doi.org/10.1190/geo2014-0269.1.
Robertsson, J.O., Blanch, J.O., Symes, W.W., 1994. Viscoelastic finite-difference modeling. Geophysics 59, 1444–1456. https://doi.org/10.1190/1.1443701.
Tam, C.K., Webb, J.C., 1993. Dispersion-relation-preserving finite difference schemes for computational acoustics. J. Comput. Phys. 107, 262–281. https://doi.org/10.1006/jcph.1993.1142.
Tan, S., Huang, L., 2014. An efficient finite-difference method with high-order accuracy in both time and space domains for modelling scalar-wave propagation. Geophys. J. Int. 197, 1250–1267. https://doi.org/10.1093/gji/ggu077.
Tarantola, A., 1984. Inversion of seismic reflection data in the acoustic approximation. Geophysics 49, 1259–1266. https://doi.org/10.1190/1.1441754.
Vigh, D., Jiao, K., Watts, D., et al., 2014. Elastic full-waveform inversion application using multicomponent measurements of seismic data collection. Geophysics 79, R63–R77. https://doi.org/10.1190/geo2013-0055.1.
Virieux, J., 1984. SH-wave propagation in heterogeneous media: velocity-stress finite-difference method. Geophysics 49, 1933–1942. https://doi.org/10.1190/1.1441605.
Virieux, J., 1986. P-SV wave propagation in heterogeneous media: velocity-stress finite-difference method. Geophysics 51, 889–901. https://doi.org/10.1190/1.1442147.
Virieux, J., Operto, S., 2009. An overview of full-waveform inversion in exploration geophysics. Geophysics 74, WCC1–WCC26. https://doi.org/10.1190/1.3238367.
Wang, E., Liu, Y., Sen, M.K., 2016. Effective finite-difference modelling methods with 2D acoustic wave equation using a combination of cross and rhombus stencils. Geophys. J. Int. 206, 1933–1958. https://doi.org/10.1093/gji/ggw250.
Wang, W., Wen, X., Tang, C., et al., 2021. Variable-order optimal implicit finite-difference schemes for explicit time-marching solutions to wave equations. Geophysics 86, T91–T106. https://doi.org/10.1190/geo2020-0239.1.
Yan, J., Sava, P., 2008. Isotropic angle-domain elastic reverse-time migration. Geophysics 73, S229–S239. https://doi.org/10.1190/1.2981241.
Yang, L., Yan, H., Liu, H., 2014. Least squares staggered-grid finite-difference for elastic wave modelling. Explor. Geophys. 45, 255–260. https://doi.org/10.1071/EG13087.
Yang, L., Yan, H., Liu, H., 2016. Optimal implicit staggered-grid finite-difference schemes based on the sampling approximation method for seismic modelling. Geophys. Prospect. 64, 595–610. https://doi.org/10.1111/1365-2478.12325.
Yang, L., Yan, H., Liu, H., 2017. Optimal staggered-grid finite-difference schemes based on the minimax approximation method with the Remez algorithm. Geophysics 82, T27–T42. https://doi.org/10.1190/geo2016-0171.1.
Zhang, J., Yao, Z., 2013a. Optimized explicit finite-difference schemes for spatial derivatives using maximum norm. J. Comput. Phys. 250, 511–526. https://doi.org/10.1016/j.jcp.2013.04.029.
Zhang, J., Yao, Z., 2013b. Optimized finite-difference operator for broadband seismic wave modeling. Geophysics 78, A13–A18. https://doi.org/10.1190/geo2012-0277.1.
Zhao, Z., Chen, J., Liu, X., et al., 2019. Frequency-domain elastic wavefield simulation with hybrid absorbing boundary conditions. J. Geophys. Eng. 16, 690–706. https://doi.org/10.1093/jge/gxz038.
Zhou, H., Liu, Y., Wang, J., 2021a. Acoustic finite-difference modeling beyond conventional Courant-Friedrichs-Lewy stability limit: approach based on variable-length temporal and spatial operators. Earthq. Sci. 34, 123–136. https://doi.org/10.29382/eqs-2021-0009.
Zhou, H., Liu, Y., Wang, J., 2021b. Elastic wave modeling with high-order temporal and spatial accuracies by a selectively modified and linearly optimized staggered-grid finite-difference scheme. IEEE Trans. Geosci. Rem. Sens. 60, 1–22. https://doi.org/10.1109/TGRS.2021.3078626.
Zhou, H., Zhang, G., 2011. Prefactored optimized compact finite-difference schemes for second spatial derivatives. Geophysics 76, WB87–WB95. https://doi.org/10.1190/geo2011-0048.1.